An Enhanced Active Disturbance Rejection Control Method for PMSM Speed Control Using Error-Corrected Cascaded ESO and Error-Transformed Adaptive RBF Neural Network

Yuxin Kang, Yongting Deng, *Senior Member, IEEE*, Chuanlong Zhai, Wenjie Li, Haiyang Cao, *Member, IEEE*, Xiufeng Liu, *Member, IEEE*, Zhimin Zhang, *Student Member, IEEE*, and Wei Xu, *Fellow, IEEE*

***Abstract*—Under complex operating conditions, permanent magnet synchronous motor (PMSM) drive systems are subject to uncertain aperiodic and periodic disturbances, which degrade speed control performance. To address this issue, this article proposes an enhanced active disturbance rejection control (ADRC) method. First, the limitations of conventional linear ADRC and its existing improvements in disturbance rejection are analyzed. Based on this, an error corrected cascaded extended state observer (EC-CESO) is proposed. Compared with traditional CESO, EC-CESO provides greater flexibility in zero placement, which enhances its ability to suppress aperiodic disturbances while reducing sensitivity to high-frequency noise. Second, an error-transformed adaptive radial basis function neural network (ET-ARBFNN) is designed to compensate for the shortcomings of EC-CESO against periodic harmonics. Unlike internal model principle-based resonant control, ET-ARBFNN requires no prior harmonic order information while achieving a significantly enhanced dynamic response. Furthermore, the disturbance rejection performance and stability of the proposed enhanced ADRC combining EC-CESO and ET-ARBFNN are analyzed. Finally, the effectiveness and superiority of the proposed method are experimentally validated on a PMSM platform.**

***Index Terms*—Active disturbance rejection control (ADRC), aperiodic and periodic disturbances, cascaded extended state observer (CESO), permanent magnet synchronous motor (PMSM), radial basis function neural network (RBFNN).**

Received 14 July 2025; revised 10 September 2025; accepted 2 October 2025. Date of publication 7 October 2025; date of current version 19 January 2026. This work was supported in part by the National Nature Science Foundation of China under Grant 12122304 and Grant 12473083, in part by the Jilin Province Key R&D Plan Project under Grant 20220203036SF, in part by the Jilin Province Science and Technology Innovation Platform Project under Grant 20230505007ZP, and in part by the Youth Innovation Promotion Association, Chinese Academy of Sciences under Grant Y2023060. Recommended for publication by Associate Editor J. Ye. *(Corresponding author: Yongting Deng.)*

Yuxin Kang, Chuanlong Zhai, Wenjie Li, and Zhimin Zhang are with the Changchun Institute of Optics, Fine Mechanics, and Physics, Chinese Academy of Sciences, Changchun 130033, China, and also with the University of Chinese Academy of Sciences, Beijing 100049, China (e-mail: kangyuxin22@mails.ucas.ac.cn; zhaichuanlong23@mails.ucas.ac.cn; liwenjie23@mails.ucas.ac.cn; zhangzhimin211@mails.ucas.ac.cn).

Yongting Deng and Xiufeng Liu are with the Changchun Institute of Optics, Fine Mechanics, and Physics, Chinese Academy of Sciences, Changchun 130033, China (e-mail: dengyongting@ciomp.ac.cn; liuxiufeng20@mails.ucas.ac.cn).

Haiyang Cao is with the Ningbo Institute of Materials Technology and Engineering, Chinese Academy of Sciences, Ningbo 315201, China (e-mail: caohaiyang@nimte.ac.cn).

Wei Xu is with the State Key Laboratory of High Density Electromagnetic Power and Systems, Institute of Electrical Engineering, Chinese Academy of Sciences, Beijing 100190, China, and also with the School of Electronic, Electrical and Communication Engineering, University of Chinese Academy of Sciences, Beijing 101408, China (e-mail: weixu@mail.iee.ac.cn).

Color versions of one or more figures in this article are available at https://doi.org/10.1109/TPEL.2025.3618670.

Digital Object Identifier 10.1109/TPEL.2025.3618670

I. Introduction

COMPARED to other types of motors, permanent magnet synchronous motor (PMSM) stands out due to its simple structure, high efficiency, high torque density, and excellent speed regulation performance [1]. Owing to these advantages, PMSM is extensively employed in advanced servo systems and other critical industrial applications that demand high dynamic performance and precise tracking [2], [3]. However, in practical applications, complex operating conditions introduce significant uncertainties, making the control system susceptible to various external and internal disturbances [4]. These disturbances can be categorized into aperiodic disturbances, such as load torque variations and motor parameters mismatches [5], and periodic disturbances, including cogging torque, current sampling errors [6], inverter nonlinearities [7], and flux linkage harmonics [8], [9]. These disturbances lead to evident aperiodic and periodic speed ripples, especially at low motor speeds [10]. Therefore, It is significantly important to suppress both aperiodic and periodic disturbances to maintain optimal performance in electric drive systems.

With the rapid development of control theory, active disturbance rejection control (ADRC), as a two-degree-of-freedom control method, has been extensively studied and applied [11], [12], [13]. ADRC enhances tracking performance and disturbance rejection capability by estimating and compensating for

the total disturbance using an extended state observer (ESO) [14]. To overcome complex tuning and stability analysis issues in early nonlinear ADRC [15], linear ADRC was proposed in [16]. By placing all ESO poles on the real axis and employing a bandwidth method, the design of controller gains and the analysis of system stability are significantly simplified. However, the inherent coupling between zeros and poles limits further performance improvement. In [12], the zero-pole coupling was decoupled by employing a weighted sum of position and speed estimation errors as the ESO input. Independent zero placement is then utilized to further improve the disturbance rejection capability of the system. Nevertheless, this method is less effective in suppressing periodic harmonic disturbances.

To simultaneously compensate for both aperiodic and periodic disturbances, various ADRC-based composite control methods have been proposed in recent years. Wang et al. [10] combined ADRC with a quasi-resonant controller (QRC) to achieve simultaneous suppression of both types of disturbances. Building on this framework, Cao et al. [17] and Wu et al. [18] introduced a cascaded ESO (CESO) by increasing the number of ESO stages, which further improved the estimation performance for aperiodic disturbances. Meanwhile, the QRC was embedded into one stage of the ESO to enable concurrent rejection of periodic harmonic disturbances. In contrast, [19], [20], and [21] proposed a generalized ESO (GESO) by extending the derivative of observed disturbance as a new observer state, thereby enhancing the estimation accuracy for aperiodic disturbances. Cui et al. [22] further cascaded the GESO with an ESO that incorporates a QRC, achieving improved aperiodic disturbance rejection while also effectively suppressing periodic disturbances. However, despite the effectiveness of the QRC in attenuating periodic harmonics at specific frequencies, it introduces undesirable peaks near those frequencies, which may lead to system instability. To address this issue, a modified resonant controller-based disturbance observer was proposed in [23]. Compared to QRC-based observers, the modified resonant controller eliminates these undesirable peaks, thereby ensuring system stability. In addition, in [24], an ESO incorporating a notch filter was designed using a cascading structure, which also avoids the undesirable peaks of the QRC. Such structures can be regarded as a form of vector resonant controller (VRC).

However, such internal model principle-based methods generally rely on the frequency information of periodic disturbances [25], which is often difficult to obtain before actual measurements. On one hand, it is challenging to identify specific periodic disturbances present during motor operation. On the other hand, theoretical models of speed fluctuations may deviate from actual situations. To effectively suppress speed fluctuations without prior knowledge of disturbance frequencies, an adaptive resonant controller was proposed in [26], which is capable of automatically identifying harmonic frequencies. However, practical systems often contain multiple harmonics. The use of multiple frequency identification terms not only increases the complexity and computational burden of the controller, but also means that the number of required identification terms remains unknown.

In recent years, the neural network-based methods have been increasingly applied in the field of disturbance observation [27], [28]. Among these, radial basis function neural networks (RBFNN) have attracted widespread attention due to their simple structure, fast learning speed, and strong approximation capability. Zhao et al. [29] proposed an online training neural network method for suppressing periodic harmonic disturbances in the current loop, where rotor position was used as the input to the network. This method was further extended in [30], broadening its applicability. However, this method requires a large number of hidden layer nodes to achieve effective suppression of periodic harmonic disturbances. As the number of nodes increases, so does the computational burden, which in turn raises the hardware requirements of the system. Liu et al. [31] and [32] are an adaptive neural network-based disturbance observer, using position error and speed error as inputs, respectively. Compared to previous approaches, this method employs fewer hidden nodes and improves the disturbance rejection performance of the controller to some extent. Nevertheless, its ability to suppress periodic harmonic disturbances is limited.

Based on the above discussion, an ADRC integrated with a RBFNN is proposed in this article. To enhance the capability of the observer in suppressing aperiodic disturbances, an error correction term is introduced into the CESO. Meanwhile, an RBFNN with an error transformation mechanism is employed to compensate for the limitation of the observer in rejecting periodic harmonics, thereby achieving high-performance speed control. The main contributions of this work are summarized as follows.

1) By introducing the estimation of the previous-stage ESO into the subsequent-stage ESO, this article proposes an error-corrected cascaded ESO (EC-CESO), which decouples the relationship between zeros and poles in the disturbance rejection transfer function of the observer. The disturbance estimation performance is further enhanced through appropriate placement of the zero locations.
2) Based on Lyapunov stability theory and by introducing an error transformation function, an error-transformed adaptive RBFNN (ET-ARBFNN) is designed to replace conventional internal-model-principle-based VRC. Leveraging the strong nonlinear approximation capability of RBFNN, the proposed method not only eliminates the dependency on known harmonic orders, enabling effective compensation of disturbances with unknown frequencies, but also significantly reduces the required number of hidden nodes compared to [30].
3) The proposed EC-CESO and ET-ARBFNN work in synergy, enabling simultaneous suppression of both aperiodic and periodic disturbances, while substantially improving the dynamic response of the system.

The rest of this article is organized as follows. In Section II, the modeling and disturbance analysis of PMSM and design of conventional ADRC is presented. Section III analyzes the limitations of existing improved methods. Section IV elaborates on the design processes of the EC-CESO and ET-ARBFNN, respectively. Section V conducts a theoretical analysis of the performance advantages of the proposed method and the system

stability. Section VI presents the experimental results, which validate the effectiveness of the proposed method. Finally, Section VII concludes this article.

II. Modeling and Disturbance Analysis of PMSM and Design of Conventional ADRC

A. Mathematical Model of PMSM

The dynamic equation of PMSM can be expressed as [8]

$$\frac{d}{dt}\omega_m = \frac{1}{J}T_e - \frac{1}{J}(T_L + B\omega_m) \tag{1}$$

where ω_m is the rotor mechanical angular velocity, J is the moment of inertia, T_L is the load torque, B is the viscous frictional coefficient, and T_e is the electromagnetic torque, which can be expressed as $T_e = K_t i_q$ when utilizing the field-oriented control strategy ($i_d = 0$) [33], where K_t is the torque coefficient, and i_d and i_q are the d- and q-axis stator currents, respectively.

B. Speed Disturbances Analysis

PMSM drives are subject to various aperiodic and periodic disturbances, as detailed in Section I. These disturbances significantly degrade speed regulation performance.

According to (1), the aperiodic disturbance d_{ap} in speed can be expressed as

$$d_{ap} = \frac{K_t - K_{t0}}{J} i_q^{\text{ref}} + \frac{K_t}{J}\left(i_q - i_q^{\text{ref}}\right) - \frac{T_L}{J} - \frac{B}{J}\omega_m + d_{un} \tag{2}$$

where K_{t0} and i_q^{ref} denote the nominal value of the torque coefficient and the reference value of the q-axis current, respectively. $(K_t - K_{t0})i_q^{\text{ref}}/J$ represents the disturbance caused by plant parameter mismatch, $K_t(i_q - i_q^{\text{ref}})/J$ denotes the disturbance due to current tracking error, T_L/J and $B\omega_m/J$ correspond to the disturbances introduced by load torque variation and viscous friction torque, respectively. In addition, d_{un} is the unknown internal and external disturbances [13].

Based on [30], the model of total periodic disturbances in the speed regulation system can be represented as the sum of multiple sinusoidal components with varying amplitudes and harmonic orders, i.e.,

$$d_{ph} = \sum_{n=1}^{\infty}\left[A_n \sin\left(k_n\omega_e t + \varphi_n\right) + A_{un}\sin\left(k_{un}\omega_e t + \varphi_{un}\right)\right] \tag{3}$$

where d_{ph} is the total periodic disturbance, ω_e is the electrical angular velocity, and n is a positive integer. k_n and k_{un} represent the known and unknown harmonic orders, respectively. When $k_n = 1, 2$, it corresponds to the periodic disturbance caused by current sampling errors; when $k_n = 6n$, it corresponds to the periodic disturbance caused by inverter nonlinearity and flux linkage harmonics, whose amplitude is typically smaller [34]. k_{un} arises from motor manufacturing imperfections and complex operating conditions [35], making its exact value difficult to obtain through theoretical modeling. A_n, A_{un}, φ_n, and φ_{un} are the corresponding amplitudes and phases, respectively.

Based on the above analysis of aperiodic and periodic disturbances in (2) and (3), the dynamic equation of the PMSM, given in (1), can be modified as

$$\frac{d}{dt}\omega_m = b_0 i_q^{\text{ref}} + d_{ap} + d_{ph} \tag{4}$$

where $b_0 = K_{t0}/J$ is the nominal control gain.

C. Design of Conventional ADRC

Taking the total disturbance d_{total} (where $d_{\text{total}} = d_{ap} + d_{ph}$) in (4) as an extended state variable, the mechanical dynamics with the total disturbance can be written in the extended state equation form as

$$\begin{cases} \dot{\omega}_m = b_0 i_q^{\text{ref}} + d_{\text{total}} \\ \dot{d}_{\text{total}} = \vartheta \end{cases} \tag{5}$$

where ϑ is the first derivative of d_{total}.

The core components of ADRC include an ESO and a linear state error feedback control law (LSEF) [17]. Based on (5), the conventional ADRC can be expressed as

$$\text{ESO: } \begin{cases} \tilde{\omega}_m = \omega_m - \hat{\omega}_m \\ \dot{\hat{\omega}}_m = b_0 i_q^{\text{ref}} + \hat{d}_{\text{total}} + \beta_1\tilde{\omega}_m \\ \dot{\hat{d}}_{\text{total}} = \beta_2\tilde{\omega}_m \end{cases}$$

$$\text{LSEF: } i_q^{\text{ref}} = \frac{1}{b_0}\left[\dot{\omega}_m^{\text{ref}} + k_p(\omega_m^{\text{ref}} - \omega_m) - \hat{d}_{\text{total}}\right] \tag{6}$$

where k_p is the gain coefficients of the controller, which is typically consistent with the bandwidth of the control loop and ω_m^{ref} represents the reference speed, $\hat{\omega}_m$ and $\hat{d}_{\text{total}}$ are the estimated values of ω_m and d_{total}, respectively. β_1 and β_2 are the gain coefficients of the ESO and are determined by the observer bandwidth ω_o. According to the pole placement method presented in [16], these gains can be designed as $\beta_1 = 2\omega_o$, $\beta_2 = \omega_o^2$.

Based on (6), the disturbance estimation transfer function $G_o^{tr}(s)$, the disturbance estimation error transfer function $G_e^{tr}(s)$, and the disturbance rejection transfer function $G_d^{tr}(s)$ can be derived as follows:

$$\begin{cases} G_o^{tr}(s) = \frac{\hat{d}_{\text{total}}(s)}{d_{\text{total}}(s)} = \frac{\omega_o^2}{(s+\omega_o)^2} \\ G_e^{tr}(s) = \frac{d_{\text{total}}(s) - \hat{d}_{\text{total}}(s)}{d_{\text{total}}(s)} = \frac{s^2 + 2\omega_o s}{(s+\omega_o)^2}. \\ G_{d1}^{tr}(s) = \frac{\omega_m(s)}{d_{\text{total}}(s)} = \frac{s^2+2\omega_o s}{(s+\omega_o)^2\cdot(s+k_p)} \end{cases} \tag{7}$$

As illustrated by the gray dashed lines in Fig. 1, which depict the Bode plots of $G_e^{tr}(s)$ and $G_o^{tr}(s)$ under varying ω_o, increasing the bandwidth improves disturbance estimation at the cost of increased sensitivity to sensor noise [17]. Consequently, the limited bandwidth of the conventional ADRC restricts its ability to adequately reject diverse disturbances.

III. Improved Design Analysis of Existing ADRCs for PMSM Speed Control Systems

A. Limitation of ADRC With CESO

The CESO enhances disturbance estimation performance by reconstructing the observer structure through increasing the

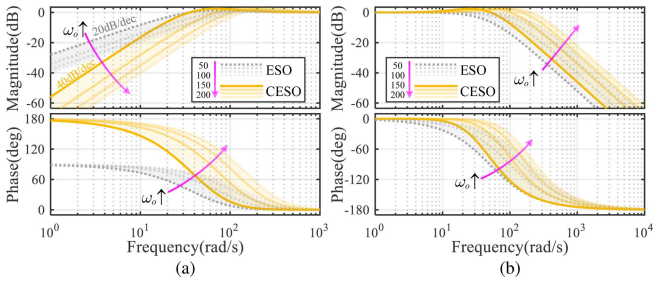

Fig. 1. Bode plots of ESO and CESO under varying ω_o. (a) $G_e^{tr}(s)$ and $G_e^{ca}(s)$. (b) $G_o^{tr}(s)$ and $G_o^{ca}(s)$.

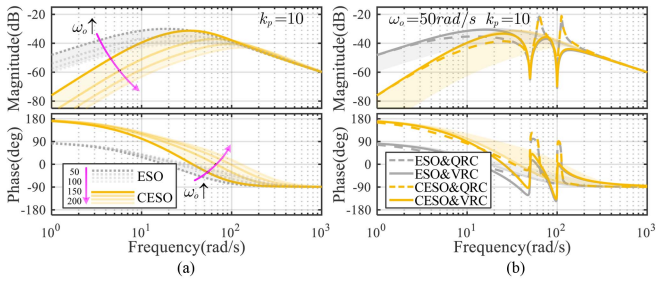

Fig. 2. Bode plots of the disturbance rejection transfer function before and after embedding the resonant controller. (a) Bode plots of $G_{d1}^{tr}(s)$ and $G_{d1}^{ca}(s)$ under different values of ω_o. (b) Bode plots of $G_{d2}^{tr}(s)$ and $G_{d2}^{ca}(s)$ with the embedded QRC and VRC.

number of ESO stages in the horizontal direction [17]. Taking the second-order CESO as an example, its structure is described as

$$\text{CESO1}\begin{cases}\tilde{\omega}_{m1}=\omega_m-\hat{\omega}_{m1}\\ \dot{\hat{\omega}}_{m1}=b_0 i_q^{\text{ref}}+\hat{d}_{\text{total1}}+\beta_{11}\tilde{\omega}_{m1}\\ \dot{\hat{d}}_{\text{total1}}=\beta_{12}\tilde{\omega}_{m1}\end{cases}$$
$$\text{CESO2}\begin{cases}\tilde{\omega}_{m2}=\omega_m-\hat{\omega}_{m2}\\ \dot{\hat{\omega}}_{m2}=b_0 i_q^{\text{ref}}+\hat{d}_{\text{total1}}+\hat{d}_{\text{total2}}+\beta_{21}\tilde{\omega}_{m2}\\ \dot{\hat{d}}_{\text{total2}}=\beta_{22}\tilde{\omega}_{m2}\end{cases}\quad(8)$$

where β_{11}, β_{12}, β_{21}, and β_{22} denote the observer gain coefficients, which can also be determined using the pole placement method as $\beta_{11}=\beta_{21}=2\omega_o$, $\beta_{12}=\beta_{22}=\omega_o^2$. $\hat{\omega}_{m1}$ and $\hat{\omega}_{m2}$ represent the estimates of the state ω_m obtained from the two cascaded stages, while $\hat{d}_{\text{total1}}$ and $\hat{d}_{\text{total2}}$ denote the partial estimates of the lumped disturbance d_{total} at each stage.

Similarly, based on the CESO structure (8), the disturbance estimation transfer function $G_o^{ca}(s)$, the disturbance estimation error transfer function $G_e^{ca}(s)$, and the disturbance rejection transfer function $G_d^{ca}(s)$ can be derived as follows:

$$\begin{cases}G_o^{ca}(s)=\frac{\hat{d}_{\text{total1}}(s)+\hat{d}_{\text{total2}}(s)}{d_{\text{total}}(s)}=\frac{2\omega_o^2 s^2+4\omega_o^3 s+\omega_o^4}{(s+\omega_o)^4}\\ G_e^{ca}(s)=\frac{d_{\text{total}}(s)-\hat{d}_{\text{total1}}(s)-\hat{d}_{\text{total2}}(s)}{d_{\text{total}}(s)}=\frac{s^2(s+2\omega_o)^2}{(s+\omega_o)^4}\\ G_{d1}^{ca}(s)=\frac{\omega_m(s)}{d_{\text{total}}(s)}=\frac{(s^2+2\omega_o s)^2}{(s+\omega_o)^4\cdot(s+k_p)}\end{cases}.\quad(9)$$

The use of a cascaded structure increases the order of the denominator in the disturbance estimation error transfer function, which improves the capability of the CESO in estimating low-frequency disturbances. As shown in Fig. 1, compared with the conventional ESO, the CESO achieves a smaller disturbance estimation error under the same bandwidth [18]. However, due to the inherent coupling between the poles and zeros of the observer, and the fact that parameter tuning is typically based on pole placement methods, the influence of zeros on observer performance is often neglected. Consequently, the improvement in low-frequency performance brought by the increased denominator order is somewhat limited.

B. Limitation of ADRC With QRC- and VRC-

High gain at specific frequencies enables the resonant controller to effectively track sinusoidal signals. It is embedded into the LSEF in (6) to suppress multiple periodic harmonic disturbances [10]. The modified LSEF can be expressed as

$$\begin{cases}G_{rcs}(s)=\sum_{\kappa=1,\ldots}\frac{\Delta_\kappa(s)}{s^2+2\omega_{c\kappa}s+\omega_{h\kappa}^2}\\ i_q^{\text{ref}}=\frac{1}{b_0}\left(\dot{\omega}_m^{\text{ref}}+[k_p+G_{rcs}(s)](\omega_m^{\text{ref}}-\omega_m)-\hat{d}_{ap}\right)\end{cases}\quad(10)$$

where κ denotes the harmonic order. When $\Delta_\kappa(s)=2k_{r\kappa}\omega_{c\kappa}s$, $G_{rcs}(s)$ corresponds to the QRC $G_{qrc}(s)$. In contrast, when $\Delta_\kappa(s)=k_{pr\kappa}s^2+k_{ir\kappa}s$, $G_{rcs}(s)$ represents the VRC $G_{vrc}(s)$. Here, $k_{r\kappa}$ is the resonant gain of QRC, $k_{pr\kappa}$ and $k_{ir\kappa}$ are the proportional and integral gains of VQC, respectively, while $\omega_{c\kappa}$ and $\omega_{h\kappa}$ denote the resonant bandwidth and resonant frequency. Accordingly, the disturbance rejection transfer function $G_d^{tr}(s)$ and $G_d^{ca}(s)$ can be reformulated as

$$\begin{cases}G_{d2}^{tr}(s)=\frac{\omega_m(s)}{d_{\text{total}}(s)}=\frac{s^2+2\omega_o s}{(s+\omega_o)^2\cdot[s+k_p+G_{rcs}(s)]}\\ G_{d2}^{ca}(s)=\frac{\omega_m(s)}{d_{\text{total}}(s)}=\frac{(s^2+2\omega_o s)^2}{(s+\omega_o)^4\cdot[s+k_p+G_{rcs}(s)]}\end{cases}.\quad(11)$$

As shown in Fig. 2, the Bode plots of the disturbance rejection transfer function after embedding the resonant controller exhibit significant magnitude attenuation at specific frequencies $\omega_{h\kappa}$, thereby suppressing harmonic disturbances within these frequencies [17]. However, QRC introduces undesirable peaks near the resonant frequencies, which not only amplify harmonic disturbance within these bands, but may also lead to system instability. In contrast, by introducing an additional term $k_{pr\kappa}s^2$ in the numerator, VRC effectively eliminates these undesirable peaks, where $k_{pi\kappa}=k_p\cdot k_{pr\kappa}$ and $k_{pr\kappa}>0$ [24]. Nevertheless, both QRC and VRC can only eliminate harmonics with known frequencies. Moreover, for systems containing multiple harmonics, multiple resonant controllers must be used in parallel, which increases the computational complexity of the control system.

IV. Proposed ADRC Speed Controller Based on ET-ARBF and EC-CESO

A. Design of the EC-CESO

To further enhance the estimation capability of the CESO for aperiodic disturbances without increasing the order of the

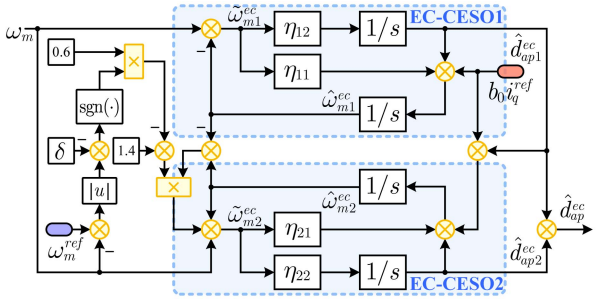

Fig. 3. Structure of the EC-CESO.

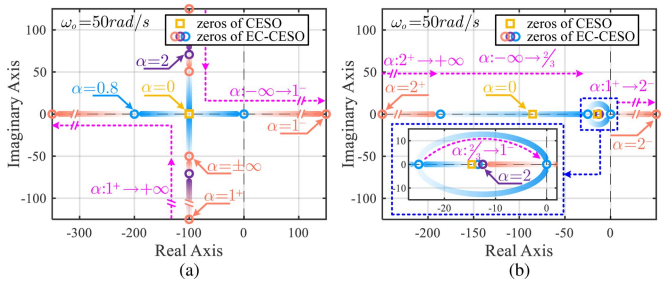

Fig. 4. Movement trajectory of zeros with varying α values. (a) zeros of $G_e^{ec}(s)$. (b) zeros of $G_o^{ec}(s)$.

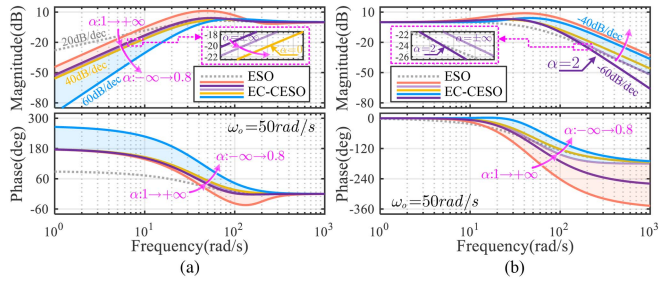

Fig. 5. Effect of the error correction term gain α on the bode plot of $G_e^{ec}(s)$ and $G_o^{ec}(s)$. (a) Bode plots of $G_e^{ec}(s)$ at different α values. (b) Bode plots of $G_o^{ec}(s)$ at different α values.

disturbance estimation function, an EC-CESO is proposed. The structure is formulated as follows:

$$\text{EC-CESO1}\begin{cases}\tilde{\omega}_{m1}^{ec} = \omega_m - \hat{\omega}_{m1}^{ec} \\ \dot{\hat{\omega}}_{m1}^{ec} = b_0 i_q^{\text{ref}} + \hat{d}_{ap1}^{ec} + \eta_{11}\tilde{\omega}_{m1}^{ec} \\ \dot{\hat{d}}_{ap1}^{ec} = \eta_{12}\tilde{\omega}_{m1}^{ec}\end{cases}$$

$$\text{EC-CESO2}\begin{cases}\tilde{\omega}_{m2}^{ec} = \omega_m - \hat{\omega}_{m2}^{ec} + \alpha(\hat{\omega}_{m2}^{ec} - \hat{\omega}_{m1}^{ec}) \\ \dot{\hat{\omega}}_{m2}^{ec} = b_0 i_q^{\text{ref}} + \hat{d}_{ap1}^{ec} + \hat{d}_{ap2}^{ec} + \eta_{21}\tilde{\omega}_{m2}^{ec} \\ \dot{\hat{d}}_{ap2}^{ec} = \eta_{22}\tilde{\omega}_{m2}^{ec}\end{cases} \tag{12}$$

where η_{11}, η_{12}, η_{21}, and η_{22} are the gain coefficients of the EC-CESO, α is the gain of the error correction term. $\hat{\omega}_{m1}^{ec}$ and $\hat{\omega}_{m2}^{ec}$ denote the estimates of ω_m obtained from the first and second cascaded stages, respectively, while $\hat{d}_{ap1}^{ec}$ and $\hat{d}_{ap2}^{ec}$ represent the partial estimates of the lumped disturbance d_{ap} at the corresponding stages. It should be noted that when $\alpha = 0$, the EC-CESO reduces to the conventional CESO. Accordingly, the block diagram of the EC-CESO is presented in Fig. 3.

Based on (5) and (12), the disturbance estimation transfer function $G_o^{ec}(s)$ of the EC-CESO can be derived as

$$G_o^{ec}(s) = \frac{\hat{d}_{ap1}^{ec}(s) + \hat{d}_{ap2}^{ec}(s)}{d_{ap}(s)} = \frac{(\eta_{22}+\eta_{12})\,s^2 + (1-\alpha)\left[(\eta_{11}\eta_{22}+\eta_{12}\eta_{21})\,s + \eta_{12}\eta_{22}\right]}{(s^2+\eta_{11}s+\eta_{12})\cdot\left[s^2+(1-\alpha)\,(\eta_{21}s+\eta_{22})\right]}. \tag{13}$$

From (13), the disturbance estimation error transfer function $G_e^{ec}(s)$ of the EC-CESO can be obtained as

$$G_e^{ec}(s) = \frac{d_{ap}(s) - \hat{d}_{ap1}^{ec}(s) - \hat{d}_{ap2}^{ec}(s)}{d_{ap}(s)} = \frac{s^4 + \left[(1-\alpha)\,\eta_{21} + \eta_{11}\right]s^3 + \left[(1-\alpha)\,\eta_{21}\eta_{11} - \alpha\eta_{22}\right]s^2}{(s^2+\eta_{11}s+\eta_{12})\cdot\left[s^2+(1-\alpha)\,(\eta_{21}s+\eta_{22})\right]}. \tag{14}$$

Similarly, the pole placement method is applied to design the gain coefficients of the EC-CESO. By setting the characteristic polynomial as $(s^2+\eta_{11}s+\eta_{12})\cdot[s^2+(1-\alpha)(\eta_{21}s+\eta_{22})] = (s+\omega_o)^4$, the gains can be obtained as $\eta_{11} = 2\omega_o$, $\eta_{12} = \omega_o^2$, $\eta_{21} = 2\omega_o/(1-\alpha)$, and $\eta_{22} = \omega_o^2/(1-\alpha)$. Consequently, (13) and (14) can be simplified to

$$\begin{cases} G_o^{ec}(s) = \frac{\left(\frac{2-\alpha}{1-\alpha}s^2+4\omega_o s+\omega_o^2\right)\omega_o^2}{(s+\omega_o)^4} \\ G_e^{ec}(s) = \frac{\left(s^2+4\omega_o s+\frac{4-5\alpha}{1-\alpha}\omega_o^2\right)s^2}{(s+\omega_o)^4} \end{cases}. \tag{15}$$

Compared with (9), an additional tunable parameter α is introduced in the zeros of $G_o^{ec}(s)$ and $G_e^{ec}(s)$, allowing for more flexibility in shaping the disturbance estimation performance. Based on (15), the zeros can be expressed, respectively, as

$$G_o^{ec}(s)\begin{cases} z_{o1} = \frac{1}{4}\omega_o & ,\ \alpha = 2 \\ z_{o1,2} = \frac{1-\alpha}{2-\alpha}\left[-2\omega_o \pm \sqrt{\frac{2-3\alpha}{1-\alpha}}\omega_o\right] & ,\ \alpha \neq 2 \end{cases}$$

$$G_e^{ec}(s)\begin{cases} z_{e1,2} = 0 \\ z_{e3,4} = -2\omega_o \pm \sqrt{\frac{\alpha}{1-\alpha}}\omega_o \end{cases}. \tag{16}$$

The trajectories of the zeros $z_{e3,4}$ and $z_{o1,2}$ with respect to varying values of α are shown in Fig. 4(a) and 4(b), respectively. Correspondingly, the Bode plots of $G_e^{ec}(s)$ and $G_o^{ec}(s)$ under different α values are presented in Fig. 5(a) and (b), respectively. As observed from Figs. 4 and 5, with the bandwidth ω_o fixed, when α increases from $-\infty$ to 0.8, the zeros $z_{e3,4}$ depart from $-2\omega_o$ and move along the real axis toward opposite directions. At the same time, the magnitude curve of $G_e^{ec}(s)$ shifts downward from left to right. When $\alpha = 0.8$, the maximum slope in the low-frequency range reaches $+60$ dB/dec. Compared with the conventional CESO, which exhibits a slope of $+40$ dB/dec, the proposed EC-CESO demonstrates a lower magnitude response

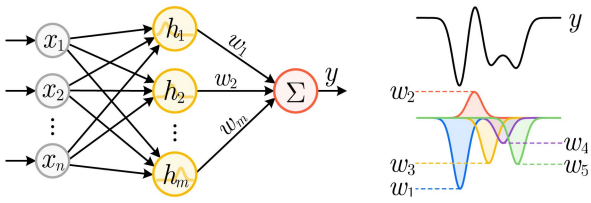

Fig. 6. Structure of the RBFNNs.

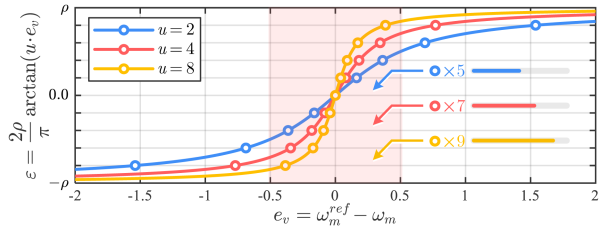

Fig. 7. Curve of transformation error ε varying with u.

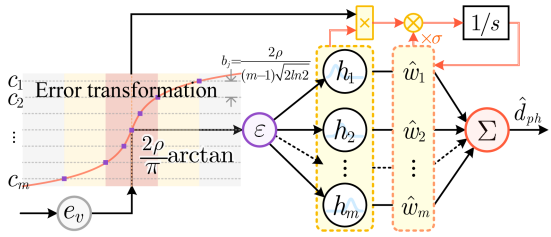

Fig. 8. Structure of the ET-ARBFNN.

at low frequencies, indicating its superior capability in attenuating low-frequency disturbances. On the other hand, when $\alpha = 2$, the zeros of $G_o^{ec}(s)$ become a single pole, and the slope of the magnitude curve of $G_o^{ec}(s)$ becomes -60 dB/dec, implying that the EC-CESO achieves stronger noise suppression performance at high frequencies under the same bandwidth. Therefore, to further balance the performance between low-frequency disturbance rejection and high-frequency noise attenuation, the following adaptive switching function is introduced:

$$\alpha = \frac{7}{5} - \frac{3}{5}\mathrm{sgn}(|e_v| - \delta) \tag{17}$$

where $e_v = \omega_m^{\mathrm{ref}} - \omega_m$ is the speed tracking error, $\mathrm{sgn}(\cdot)$ is the sign function[36], and δ is the switching threshold, which is typically set to the amplitude of the steady-state fluctuations of ω_m. When the system is in dynamic state, i.e., $|e_v| > \delta$, α is set to 0.8 to achieve stronger disturbance rejection performance. Conversely, when the system approaches steady state, i.e., $|e_v| < \delta$, α switches to 2 to enhance noise suppression performance.

B. LSEF Based on ET-ARBFNN

The structure of the RBFNNs is illustrated in Fig. 6. It consists of an input layer $\boldsymbol{x} = [x_1, x_2, \ldots, x_n]^{\mathrm{T}}$, a hidden layer $\boldsymbol{h} = [h_1, h_2, \ldots, h_m]^{\mathrm{T}}$, and an output layer y. Each neuron in the hidden layer employs an RBF, and the output layer computes the weighted sum of the hidden layer outputs, where w_i denotes the weight associated with the ith RBF neuron. As illustrated in Fig. 6, an RBF typically takes the form of a bell-shaped curve. Therefore, geometrically speaking, RBF neural networks work by combining multiple such bell-shaped curves to reconstruct a target function. Since each neuron in the hidden layer corresponds to one RBF, the number of hidden neurons directly determines the count of RBFs used in the reconstruction.

It is evident that the approximation capability of a neural network increases with the number of hidden layer neurons. However, the practical selection of this number is limited by the computational resources available on the processor. Without increasing the number of neurons, reducing the spacing between them may also improve local approximation accuracy. Nevertheless, dynamically adjusting the centers and widths of each neuron would significantly increase the computational burden. To address this limitation, this article proposes an adaptive RBFNN based on error transformation (ET-ARBFNN). An error transformation function $S(\varepsilon)$ is introduced, which satisfies the following properties:

1) $S(\varepsilon)$ is a strictly increasing smooth function;
2) $S(\varepsilon)$ is an odd function, and $\lim_{\varepsilon \to \mathrm{sgn}(e_v)\rho} S(\varepsilon) = \mathrm{sgn}(e_v) \cdot \infty$

where ρ is a positive real constant, and ε is referred to as the transformed error. $S(\varepsilon)$ is selected as

$$S(\varepsilon) = \frac{1}{u} \cdot \tan\left(\frac{\pi}{2\rho}\varepsilon\right). \tag{18}$$

Since $S(\varepsilon)$ is strictly monotonically increasing, let $e_v = S(\varepsilon)$, the inverse transformation exists and can be expressed as

$$\varepsilon = S^{-1}(e) = \frac{2\rho}{\pi}\arctan\left(u \cdot e_v\right) \tag{19}$$

where u is the approximation factor. As shown in Fig. 7, within the same error range, increasing u encourages more nodes to participate in the approximation process, which helps improve approximation performance. However, an excessively large u may cause overshoot and overfitting [37], affecting system stability. By using ε as the input to the neural network, an ET-ARBFNN is obtained, whose structure is illustrated in Fig. 8. In each neuron of the hidden layer, the Gaussian function is employed and expressed as

$$h_j = \exp\left(-\frac{\|\varepsilon - c_j\|_2^2}{2b_j^2}\right) \tag{20}$$

where h_j, b_j, and c_j represent the output, width, and center of the jth neuron in the hidden layer, respectively. Given that the network input is bounded within the interval $\varepsilon \in (-\rho, \rho)$, the centers c_j can be selected directly from this range. Specifically, they are uniformly distributed across the input domain based on the number of hidden neurons m, i.e., evenly spaced from $-\rho$ to ρ. Once the centers c_j are determined, the corresponding widths b_j are also fixed as $b_j = \frac{2\rho}{(m-1)\sqrt{2\ln 2}}$ [38], which helps accelerate the training process and reduce the computational burden.

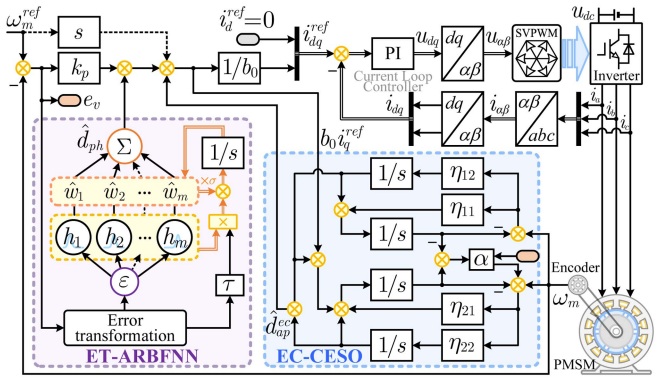

Fig. 9. Structure of the proposed PMSM speed control method combining EC-CESO and ET-ARBFNN.

Thus, the harmonic disturbances approximated by the ET-ARBFNN can be expressed as

$$\hat{d}_{ph} = \sum_{i=1}^{m} \hat{w}_i h_i = \hat{\boldsymbol{w}}^{\mathrm{T}} \boldsymbol{h} \tag{21}$$

where $\hat{\boldsymbol{w}}$ denotes the adaptive weight vector.

The periodic harmonic disturbance d_{ph} in (4) can also be expressed in the same form as

$$d_{ph} = \boldsymbol{w}^{\mathrm{T}} \boldsymbol{h} + \xi \tag{22}$$

where $\boldsymbol{w}$ represents the ideal weight vector, and ξ denotes the approximation error, which is bounded by a positive constant as $|\xi| < \xi_b$.

To ensure that $\hat{\boldsymbol{w}}$ converges to $\boldsymbol{w}$, the weight adaptive law is designed as [30]

$$\dot{\hat{\boldsymbol{w}}} = -\tau e_v \boldsymbol{h} - \sigma \hat{\boldsymbol{w}} \tag{23}$$

where $\tau > 0$ denotes the gain coefficient and σ is a small positive constant.

Taking the derivative of the speed tracking error $e_v = \omega_m^{\mathrm{ref}} - \omega_m$ and substituting (4) into it, we can obtain

$$\dot{e}_v = \dot{\omega}_m^{\mathrm{ref}} - b_0 i_q^{\mathrm{ref}} + d_{ap} + d_{ph}. \tag{24}$$

The feedback control law of tracking error is applied as

$$\dot{e}_v = -k_p e_v. \tag{25}$$

Then, based on (12) and (21), substituting $\hat{d}_{ap}$ and $\hat{d}_{ph}$ for d_{ap} and d_{ph}, respectively, and inserting (25) into (24), the improved LSEF can be expressed as

$$i_q^{\mathrm{ref}} = \frac{1}{b_0}\left[\dot{\omega}_m^{\mathrm{ref}} + k_p e_v - \hat{\boldsymbol{w}}^{\mathrm{T}} \boldsymbol{h} - \hat{d}_{ap}\right]. \tag{26}$$

Finally, the structure of the proposed PMSM speed control method combining EC-CESO and ET-ARBFNN is shown in Fig. 9, where a PI controller is applied in the current loop.

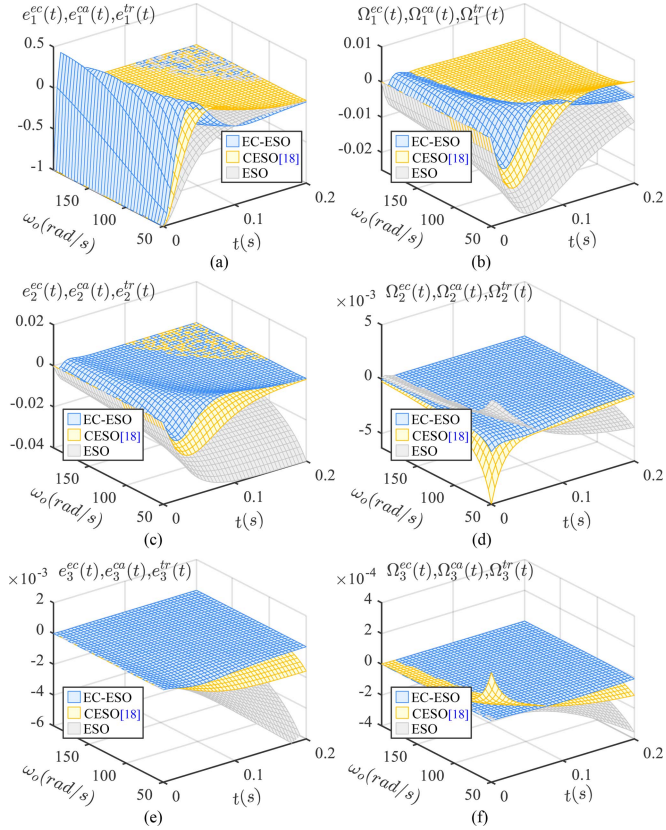

Fig. 10. Comparison of time-domain responses for three types of observers and their corresponding controllers under different values of ω_o, subjected to various disturbances. The left side shows the comparison among ESO, CESO[18], and EC-CESO, while the right side compares the corresponding controllers, where $k_p = 10$. (a) and (b) for $d_{ap}(t) = R \cdot 1(t)$. (c) and (d) for $d_{ap}(t) = Rt$. (e) and (f) for $d_{ap}(t) = Rt^2/2$.

V. Performance Analysis

A. Aperiodic Disturbance Estimation Analysis of EC-CESO

To demonstrate the superiority of the proposed EC-CESO in estimating aperiodic disturbance, this subsection provides a comparative analysis of ESO, CESO [18], and EC-CESO from both the time domain and frequency domain perspectives.

When the disturbance $d_{ap}(t)$ is a step signal $R \cdot 1(t)$, a ramp signal Rt, or an acceleration signal $Rt^2/2$, the dynamic outputs $e_1(t)$, $e_2(t)$, and $e_3(t)$ of ESO, CESO, and EC-CESO, along with their corresponding ADRC outputs $\Omega_1(t)$, $\Omega_2(t)$, and $\Omega_3(t)$ can be obtained from (7), (9), and (15), respectively, as shown in Fig. 10. It can be observed that for a step signal $d_{ap}(t) = R \cdot 1(t)$, all three types of observers and their corresponding controllers exhibit no steady-state error. For the ramp signal $d_{ap}(t) = Rt$, both ESO and its corresponding controller show steady-state errors, whereas the proposed EC-CESO and CESO, along with their respective controllers, are capable of converging to zero. For the acceleration signal $d_{ap}(t) = Rt^2/2$, only the EC-CESO is able to converge to zero. The steady-state disturbance estimation errors of the three types of observers are summarized in Table I. This indicates that the proposed scheme,

TABLE I
STEADY-STATE ESTIMATION ERRORS FOR DIFFERENT DISTURBANCES

	Step signal $R\cdot 1(t)$	Ramp signal Rt	Acceleration signal $Rt^2/2$
$e_i^{tr}(\infty)$ of ESO	0	$2R/\omega_o$	∞
$e_i^{ca}(\infty)$ of CESO [18]	0	0	$4R/\omega_o^2$
$e_i^{ec}(\infty)$ of EC-CESO	0	0	0

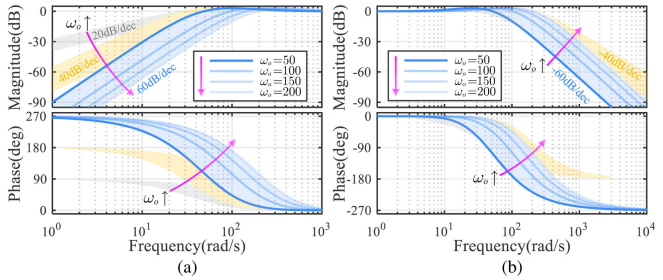

Fig. 11. Bode plots of EC-CESO under varying ω_o. (a) $G_e^{ec}(s)$. (b) $G_o^{ec}(s)$.

by introducing an error correction term, eliminates the response error caused by acceleration disturbances, thereby achieving a higher level of disturbance estimation accuracy and enhancing disturbance rejection capability.

To further intuitively illustrate the influence of ω_o on disturbance estimation, the same parameters as those in Fig. 1 are selected. The Bode plots of $G_e^{ec}(s)$ and $G_o^{ec}(s)$ under different values of ω_o are shown in Fig. 11. It can be observed that both the disturbance estimation error magnitude curve and the noise suppression magnitude curve of the EC-CESO exhibit a slope of 60 dB/dec. Therefore, it can be concluded that when the same ω_o is adopted, the EC-CESO achieves superior disturbance rejection performance at low frequencies and better noise suppression performance at high frequencies compared to the conventional CESO.

B. Periodic Disturbance Estimation Analysis of ET-ARBFNN

To demonstrate the superiority of ET-ARBFNN in estimating periodic disturbances, this section presents a theoretical analysis of its approximation performance. As described in Section IV-B, the approximation accuracy of the RBF neural network is directly determined by the number of its nodes and the width parameter b_j. The Gaussian basis function can be approximately regarded as half a cycle of a sine wave $\sin(\omega_h t)$. Therefore, the maximum frequency of the periodic harmonic disturbance that can be approximated almost completely by RBFNN is given by

$$\omega_{h-\max}=\frac{1}{2b_j}=\frac{(m-1)\sqrt{2\ln 2}}{4\rho}. \tag{27}$$

According to the frequency sweep method, as the harmonic frequency continues to increase, the ET-ARBFNN still maintains a certain approximation capability. However, when the frequency exceeds four times $\omega_{h-\max}$, the approximation performance begins to show some degree of amplitude attenuation. The frequency sweep simulation result is shown in Fig. 12.

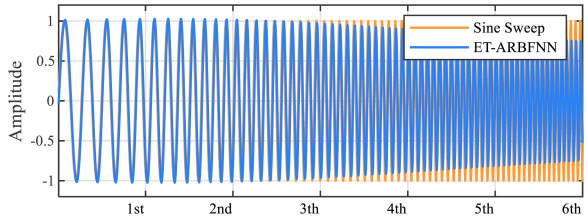

Fig. 12. Simulation of ET-ARBFNN approximation capability.

C. Stability and Convergence Analysis

According to (5) and (12), the estimation error of EC-CESO can be derived as

$$\begin{cases}\dot{\tilde{\omega}}_{m1}^{ec}=\tilde{d}_{ap1}^{ec}-\eta_{11}\tilde{\omega}_{m1}^{ec}\\ \dot{\tilde{d}}_{ap1}^{ec}=\dot{d}_{ap}-\dot{\hat{d}}_{ap1}^{ec}=\vartheta-\eta_{12}\tilde{\omega}_{m1}^{ec}\\ \dot{\tilde{\omega}}_{m2}^{ec}=\tilde{d}_{ap2}^{ec}-(1-\alpha)\eta_{21}\tilde{\omega}_{m2}^{ec}-\alpha\eta_{11}\tilde{\omega}_{m1}^{ec}\\ \dot{\tilde{d}}_{ap2}^{ec}=\dot{d}_{ap}-\dot{\hat{d}}_{ap1}^{ec}-(1-\alpha)\dot{\hat{d}}_{ap2}^{ec}\\ \qquad\quad=\vartheta-\eta_{12}\tilde{\omega}_{m1}^{ec}-(1-\alpha)\eta_{22}\tilde{\omega}_{m2}^{ec}\end{cases}. \tag{28}$$

Let $e_1=\tilde{\omega}_{m1}^{ec}$, $e_2=\tilde{d}_{ap1}^{ec}/\omega_o$, $e_3=\tilde{\omega}_{m2}^{ec}$, and $e_4=\tilde{d}_{ap2}^{ec}/\omega_o$, then (28) can be rewritten as

$$\dot{\boldsymbol{e}}=\omega_o\boldsymbol{A}\boldsymbol{e}+\frac{\vartheta}{\omega_o}\boldsymbol{B} \tag{29}$$

where $\boldsymbol{e}=\begin{bmatrix}e_1\\e_2\\e_3\\e_4\end{bmatrix}$, $\boldsymbol{A}=\begin{bmatrix}-2&1&0&0\\-1&0&0&0\\-2\alpha&0&-2&1\\-1&0&-1&0\end{bmatrix}$, $\boldsymbol{B}=\begin{bmatrix}0\\1\\0\\1\end{bmatrix}$.

Both eigenvalues of $\boldsymbol{A}$ are -1, so $\boldsymbol{A}$ is Hurwitz stable. Then, there exists a unique positive definite matrix $\boldsymbol{P}$ such that

$$\boldsymbol{A}^{\mathrm{T}}\boldsymbol{P}+\boldsymbol{P}\boldsymbol{A}=-\boldsymbol{Q} \tag{30}$$

where $\boldsymbol{Q}$ is a positive definite symmetric matrix. Let $\boldsymbol{Q}=\mathrm{diag}(1,1,1,1)$, then $\boldsymbol{P}$ can be obtained as

$$\boldsymbol{P}=\begin{bmatrix}\frac{\alpha-\alpha^2}{4}-\frac{11}{16}&\frac{1}{2}&\frac{\alpha}{4}-\frac{1}{8}&\frac{3}{8}-\frac{\alpha}{4}\\ \frac{1}{2}&\frac{5\alpha-3\alpha^2}{4}-\frac{37}{16}&\frac{\alpha}{4}-\frac{3}{8}&\frac{5}{8}-\frac{\alpha}{4}\\ \frac{\alpha}{4}-\frac{1}{8}&\frac{\alpha}{4}-\frac{3}{8}&-\frac{1}{2}&\frac{1}{2}\\ \frac{3}{8}-\frac{\alpha}{4}&\frac{5}{8}-\frac{\alpha}{4}&\frac{1}{2}&-\frac{3}{2}\end{bmatrix}. \tag{31}$$

Select the Lyapunov function as $V_0(\boldsymbol{e})=\boldsymbol{e}^{\mathrm{T}}\boldsymbol{P}\boldsymbol{e}$, and then

$$\dot{V}_0=\dot{\boldsymbol{e}}^{\mathrm{T}}\boldsymbol{P}\boldsymbol{e}+\boldsymbol{e}^{\mathrm{T}}\boldsymbol{P}\dot{\boldsymbol{e}}=-\omega_o\|\boldsymbol{e}\|_2^2+2\vartheta\omega_o^{-1}\boldsymbol{e}^{\mathrm{T}}\boldsymbol{P}\boldsymbol{B}. \tag{32}$$

Since ϑ satisfies the Lipschitz condition within its domain, there exists a constant ζ such that $|\vartheta|\leqslant\zeta\|\tilde{\omega}_{mi}^{ec};\tilde{d}_{api}^{ec}\|_2$ holds, where $i=1,2$. Thus, the following expression can be derived:

$$2\vartheta\omega_o^{-1}\boldsymbol{e}^{\mathrm{T}}\boldsymbol{P}\boldsymbol{B}\leqslant 2\zeta\omega_o^{-1}\boldsymbol{e}^{\mathrm{T}}\boldsymbol{P}\boldsymbol{B}\left\|\tilde{\omega}_{mi}^{ec};\tilde{d}_{api}^{ec}\right\|_2. \tag{33}$$

when $\omega_o\geqslant 1$, the following equation is obtained:

$$\omega_o^{-1}\left\|\tilde{\omega}_{mi}^{ec};\tilde{d}_{api}^{ec}\right\|_2=\omega_o^{-1}\sqrt{e_1^2+\omega_o^2e_2^2+e_3^2+\omega_o^2e_4^2}\leqslant\|\boldsymbol{e}\|_2. \tag{34}$$

Substituting (33) and (34) into (32), we can get

$$\begin{aligned}\dot{V}_0 &= -\omega_o\|\boldsymbol{e}\|_2^2 + 2\vartheta\omega_o^{-1}\boldsymbol{e}^{\mathrm{T}}\boldsymbol{P}\boldsymbol{B}\\ &\leqslant -\omega_o\|\boldsymbol{e}\|_2^2 + 2\zeta\boldsymbol{e}^{\mathrm{T}}\boldsymbol{P}\boldsymbol{B}\|\boldsymbol{e}\|_2\\ &\leqslant -\omega_o\|\boldsymbol{e}\|_2^2 + \left(\|\zeta\boldsymbol{P}\boldsymbol{B}\|_2^2+1\right)\|\boldsymbol{e}\|_2^2. \end{aligned} \tag{35}$$

It can be observed that $\dot{V}_0 < 0$ when $\omega_o > \|\zeta\boldsymbol{P}\boldsymbol{B}\|_2^2 + 1$. Based on Lyapunov stability theory, it can be concluded that $\lim_{t\to\infty}\tilde{\omega}_{mi}^{ec} = 0$ and $\lim_{t\to\infty}\tilde{d}_{api}^{ec} = 0$, indicating that the estimation error of the EC-CESO asymptotically approaches zero as time progresses. Consequently, the proposed observer is stable. Then, substituting (22) and (26) into (4) yields

$$\dot{e}_v = -k_p e_v - \tilde{\boldsymbol{w}}^{\mathrm{T}}\boldsymbol{h} - \xi \tag{36}$$

where $\tilde{\boldsymbol{w}} = \boldsymbol{w} - \hat{\boldsymbol{w}}$. After embedding the ET-ARBFNN, to verify the feasibility of the proposed control method, the following Lyapunov function is chosen as

$$V = \frac{1}{2}e_v^2 + \frac{1}{2\tau}\tilde{\boldsymbol{w}}^{\mathrm{T}}\tilde{\boldsymbol{w}} \tag{37}$$

then the derivative of (37) can be deduced as

$$\dot{V} = e_v\dot{e}_v + \frac{1}{\tau}\tilde{\boldsymbol{w}}^{\mathrm{T}}\dot{\tilde{\boldsymbol{w}}}. \tag{38}$$

When the neural network is perfectly trained, the optimum weight vector $\boldsymbol{w}$ is supposed to be constant. Thus, its derivative can be regarded as zero, i.e., $\dot{\boldsymbol{w}} = 0$. Then substituting (23) and (36) into (38), it can be further expressed as

$$\begin{aligned}\dot{V} &= -k_p e_v^2 - e_v\tilde{\boldsymbol{w}}^{\mathrm{T}}\boldsymbol{h} - e_v\xi - \frac{1}{\tau}\tilde{\boldsymbol{w}}^{\mathrm{T}}\dot{\hat{\boldsymbol{w}}}\\ &= -k_p e_v^2 - e_v\xi + \frac{\sigma}{\tau}\tilde{\boldsymbol{w}}^{\mathrm{T}}\hat{\boldsymbol{w}} \end{aligned} \tag{39}$$

Further, using Young's inequality $\pm\boldsymbol{a}^{\mathrm{T}}\boldsymbol{b} \leqslant \frac{1}{2}\boldsymbol{a}^{\mathrm{T}}\boldsymbol{a} + \frac{1}{2}\boldsymbol{b}^{\mathrm{T}}\boldsymbol{b}$ [27] can yield

$$\begin{aligned}\frac{\sigma}{\tau}\tilde{\boldsymbol{w}}^{\mathrm{T}}\hat{\boldsymbol{w}} &= \frac{\sigma}{\tau}\tilde{\boldsymbol{w}}^{\mathrm{T}}\boldsymbol{w} - \frac{\sigma}{\tau}\tilde{\boldsymbol{w}}^{\mathrm{T}}\tilde{\boldsymbol{w}}\\ &\leqslant -\frac{\sigma}{2\tau}\tilde{\boldsymbol{w}}^{\mathrm{T}}\tilde{\boldsymbol{w}} + \frac{\sigma}{2\tau}\|\boldsymbol{w}\|_2^2\\ -e_v\xi &\leqslant \frac{1}{2}e_v^2 + \frac{1}{2}\xi_b^2. \end{aligned} \tag{40}$$

After substituting (40) into (39), the following expression is obtained:

$$\begin{aligned}\dot{V} &\leqslant -\left(k_p - \frac{1}{2}\right)e_v^2 + \frac{1}{2}\xi_b^2 - \frac{\sigma}{2\tau}\tilde{\boldsymbol{w}}^{\mathrm{T}}\tilde{\boldsymbol{w}} + \frac{\sigma}{2\tau}\|\boldsymbol{w}\|_2^2\\ &\leqslant -aV + f \end{aligned} \tag{41}$$

where $a = \min\{2k_p - 1, \sigma\}$ and $f = \frac{\sigma}{2\tau}\|\boldsymbol{w}\|_2^2 + \frac{1}{2}\xi_b^2$. According to [30], (41) can be solved as

$$V(t) \leqslant \left[V(0) - \frac{f}{a}\right]e^{-at} + \frac{f}{a}. \tag{42}$$

As long as $a > 0$, $V(t)$ converges exponentially to f/a. In other words, the speed tracking error and the disturbance observation error asymptotically converge to a small neighborhood around zero. Therefore, it can be concluded that the proposed speed control system remains stable.

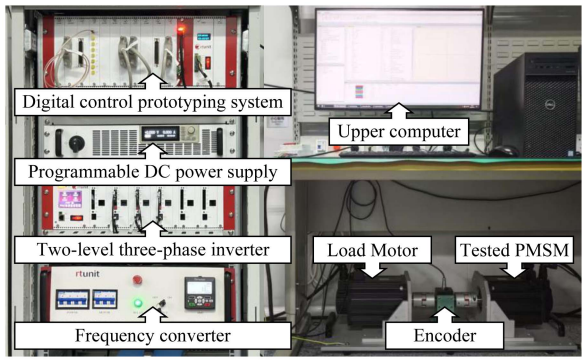

Fig. 13. Experimental hardware platform.

TABLE II
PARAMETERS OF PMSM DRIVES

Parameters	Value	Parameters	Value
Stator inductance L_s	0.65mH	DC-bus voltage u_{dc}	400V
Stator resistance R_s	0.12Ω	Rated voltage u_n	220V
Rotor flux linkage ψ_f	0.1754Wb	Rated torque T_L	20N·m
Total Inertia J	0.028kg·m^2	Pole pairs p_n	4

VI. EXPERIMENTAL VERIFICATION

The experiments are performed using the TMS320C28346 DSP-based digital control system. The rotation speed and rotor position are measured by an incremental photoelectric encoder with a resolution of 2500. The load motor is connected to the tested PMSM through plum coupling, and the load is controlled by a frequency converter. The dc bus voltage is powered by a programmable dc power source and set to 400 V. Both the inverter switching and sampling frequency are set to 10 kHz. The picture of the experimental platform is presented in Fig. 13, and the specifications of the tested PMSM are detailed in Table II.

To comprehensively evaluate the effectiveness of the proposed method, its performance in suppressing both aperiodic and periodic disturbances is compared. The conventional ESO-ADRC and the CESO-ADRC from [18] are selected as benchmark methods to verify the effectiveness of the proposed EC-CESO in aperiodic disturbance rejection. Furthermore, since the VRC derived from [24] further addresses the shortcomings of QRC and demonstrates excellent performance in suppressing periodic disturbances with known frequencies, it is selected in this article as a comparative method to evaluate the effectiveness of the proposed ET-RBFNN in periodic disturbance suppression. To ensure a fair comparison, all methods share the same common parameters, while the unique parameters are tuned to their respective near-optimal values individually. According to [34], the resonant frequencies of the VRC are chosen as $\omega_{h1} = \omega_e$ and $\omega_{h2} = 2\omega_e$, while the other parameters are set to $\omega_{c1,2} = 2\%\omega_{h1,2}$, $k_{pr1,2} = 10$, and $k_{pi1,2} = 10k_{pr1,2}$ [24]. The controller gain k_p is set to 10, and the observer bandwidth ω_o is determined using the positive bandwidth allocation method

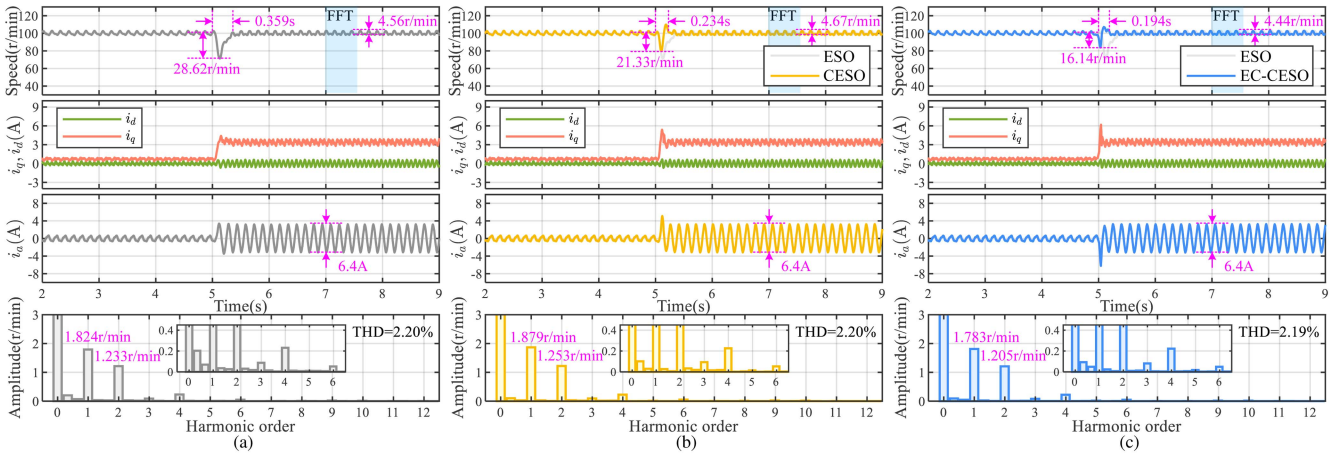

Fig. 14. Experimental results of speed, dq-axis currents, phase-a current, and FFT analysis of steady-state speed at 100 r/min under sudden load disturbance of 3 N · m using three different control methods. (a) ESO-ADRC. (b) CESO-ADRC. (c) EC-CESO-ADRC.

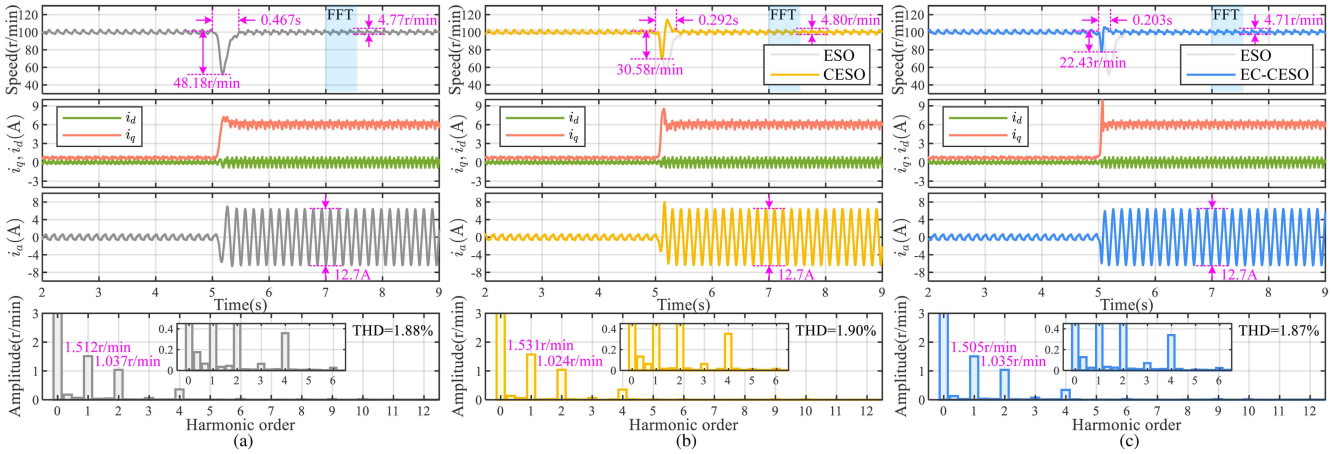

Fig. 15. Experimental results of speed, dq-axis currents, phase-a current, and FFT analysis of steady-state speed at 100 r/min under sudden load disturbance of 6 N · m using three different control methods. (a) ESO-ADRC. (b) CESO-ADRC. (c) EC-CESO-ADRC.

from [16] as 50 rad/s (five times the value of k_p). While the switching threshold δ of the proposed EC-CESO is set to 0.5, and the parameters of the proposed ET-ARBFNN are set to $u = 2$, $\tau = 150$, $\sigma = 10^{-5}$, $m = 11$, $\rho = 0.5$, $b_j = 0.085$, $c_j = [-0.5 : 0.1 : 0.5]$. According to the findings in [10], speed harmonics are more prominent during low-speed operation. Therefore, the reference speed is set to 100 r/min to better highlight the disturbance rejection capability of the proposed method under such operating conditions.

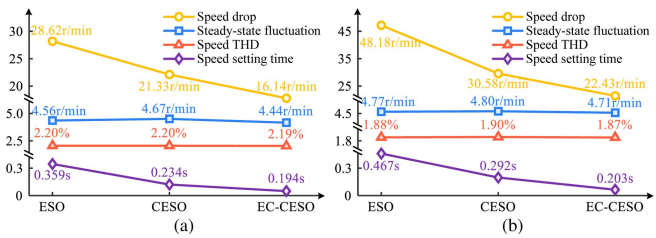

Fig. 16. Performance comparison of ESO, CESO, and EC-CESO at 100 r/min under 3 and 6 N · m loads. (a) 3 N · m load. (b) 6 N · m load.

A. *Disturbance Suppression Performance Experiment*

To evaluate the disturbance rejection performance of the three observers, Figs. 14 and 15 present the system responses under sudden load disturbance of 3 and 6 N · m, including the speed, dq-axis currents, and phase-a current waveforms obtained using different observers.

As shown in Fig. 14(b), with the CESO-ADR method, the steady-state speed fluctuation is 4.67 r/min. When a 3 N · m load is suddenly applied, the speed drops instantaneously by 21.33 r/min, and the system takes approximately 0.234 s to return to steady state. Compared to the traditional ESO-ADRC method in Fig. 14(a), where the instantaneous speed drop is 28.62 r/min and the setting time is 0.359 s, the CESO-ADRC reduces the speed drop by 25.5% and shortens the setting time by 34.8%. However, no significant improvement is observed

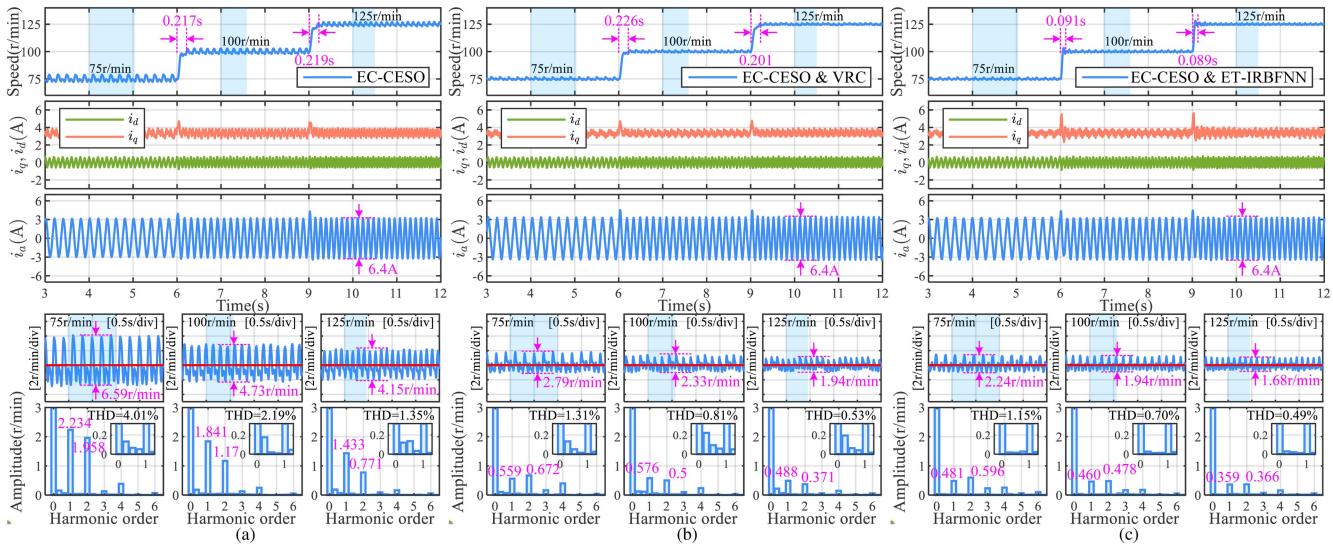

Fig. 17. Experimental results of speed, dq-axis currents, phase-a current, and FFT analysis of steady-state speed at 3 N · m load under variable speed. (a) EC-CESO-ADRC. (b) EC-CESO & VRC-ADRC. (c) EC-CESO & ET-ARBFNN-ADRC.

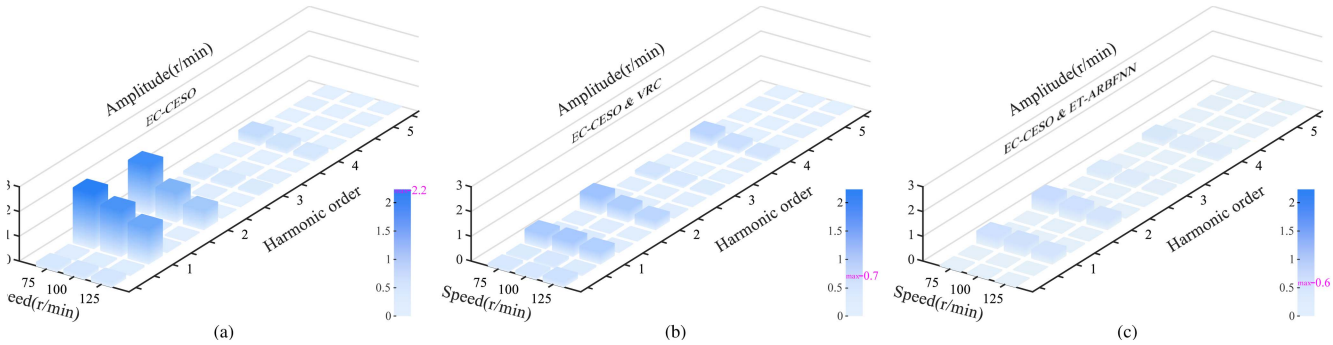

Fig. 18. Experimental results of FFT analysis at different speeds. (a) EC-CESO-ADRC. (b) EC-CESO & VRC-ADRC. (c) EC-CESO & ET-ARBFNN-ADRC.

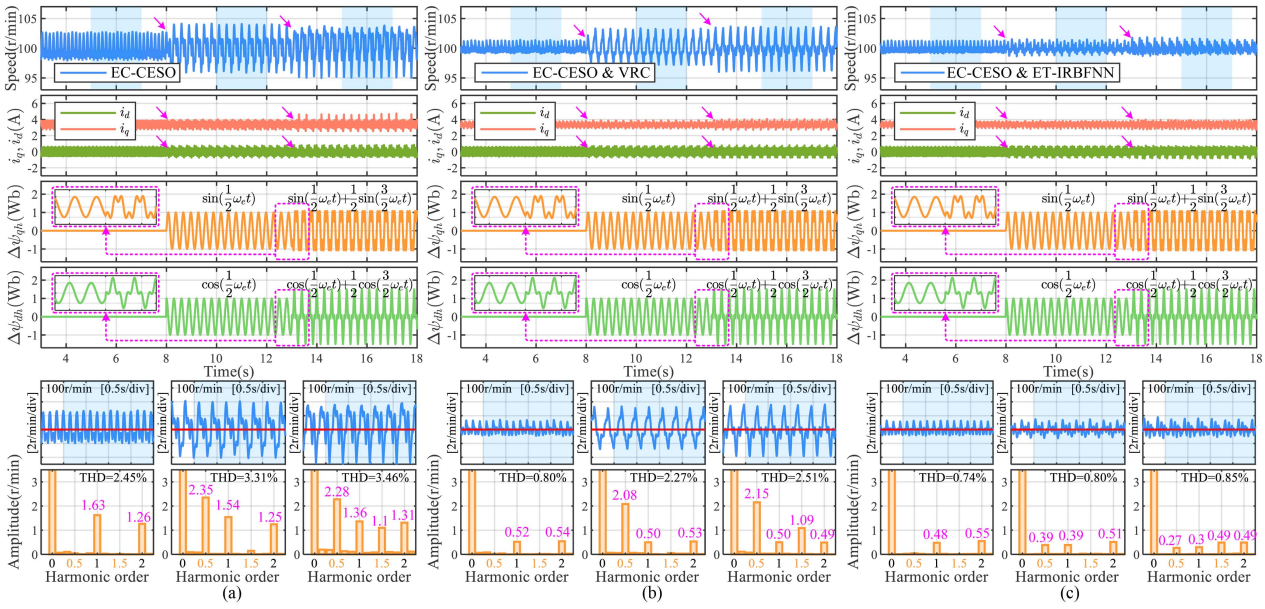

Fig. 19. Experimental results of speed, dq-axis currents, periodic disturbances, and FFT analysis of steady-state speed at 3 N · m load under periodic disturbances of specific frequencies. (a) EC-CESO-ADRC. (b) EC-CESO & VRC-ADRC. (c) EC-CESO & ET-ARBFNN-ADRC.

in the steady-state fluctuation. Fig. 14(c) shows that with the proposed EC-CESO-ADRC method, the steady-state fluctuation is reduced to 4.44 r/min, indicating a slight improvement over the CESO-ADRC. Under the same 3 N · m load, the instantaneous speed drop is further reduced to 16.14 r/min, and the setting time is shortened to 0.194 s. Compared to the conventional ESO-ADRC, this represents a 43.6% reduction in speed drop and a 46.0% decrease in setting time.

Similarly, the experimental results under a 6 N · m load are shown in Fig. 15, where the response trends are generally consistent with those observed in Fig. 14.

For the sake of comparison, Fig. 16 presents the experimental results of the ADRC control methods based on three different observers. It shows that the proposed EC-CESO, by introducing an error correction term into the CESO framework, not only reduces the speed drop caused by sudden load disturbance, but also significantly shortens the setting time, thereby enhancing the capability of the system to reject aperiodic disturbance. This result is consistent with the theoretical analysis presented in Section IV-A. Although the steady-state performance is improved, the steady-state fluctuations are still noticeable, indicating that further optimization is required to effectively suppress periodic harmonics.

B. Experimental Results Under Variable Speed

Since the superior performance of EC-CESO in suppressing aperiodic disturbance has been verified in the previous section, EC-CESO is uniformly adopted as the aperiodic disturbance observer in this section, and is compared with EC-CESO & VRC and the proposed EC-CESO & ET-ARBFNN. As the periodic disturbance in the speed loop consist of multiple harmonic components, the characteristics of speed fluctuations vary under different reference speeds. Therefore, the variable-speed experiment is conducted under 3 N · m load, where the reference speed is sequentially set to 75, 100, and 125 r/min, with an increment of 25 r/min each time. The experimental results are shown in Fig. 17. Based on the FFT analysis during the steady-state speed, the amplitudes of speed harmonics at different harmonic orders under different speeds are graphically illustrated in Fig. 18.

Fig. 17(a) illustrates both the steady-state and dynamic performance of EC-CESO-ADRC across various speed stages, along with the corresponding FFT analysis of the speed. The controller demonstrates rapid response and effective elimination of speed tracking errors when the reference speed changes. Nevertheless, notable speed fluctuations persist during steady-state operation, which is consistent with the conclusion drawn in the previous section. The FFT results reveal that the dominant harmonic components are primarily concentrated at the 1st and 2nd harmonics of the fundamental speed frequency. In addition, several noninteger-order harmonics are observed between the dc component and the first harmonic.

In comparison, as shown in Fig. 17(b) and 17(c), the integration of VRC or the proposed ET-ARBFNN method significantly reduces speed fluctuations across all tested speed stages. For harmonics with unknown orders (noninteger-order harmonics serve as an example), VRC achieves almost no suppression effect, whereas the proposed ET-ARBFNN demonstrates strong

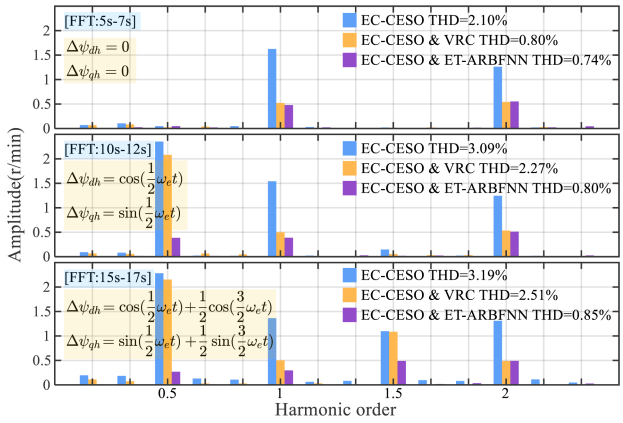

Fig. 20. Experimental results of FFT analysis of the speed under three different control methods.

capability in attenuating such disturbances. This further highlights the superior performance of the proposed method in rejecting periodic disturbance.

Furthermore, since the neural network suppresses disturbance through an approximation mechanism, sudden changes in speed can be treated as external disturbance. As shown in Fig. 17, ET-ARBFNN not only effectively attenuates harmonic disturbances under steady-state, but also significantly improves the dynamic response of the system. Specifically, the setting time is reduced by approximately 50%. In contrast, the VRC has minimal impact on the it, and in some cases leads to deterioration.

C. Experimental Results Under Periodic Disturbances of Specific Frequencies

To further validate the superiority of the ET-RBFNN in suppressing uncertain periodic disturbances, experiments involving sudden injection of periodic disturbances at different frequencies were conducted under a 3 N · m load condition. Specifically, periodic signals with frequencies of 0.5 and 1.5 times the fundamental frequency were injected into the dq-axis at 8 and 13 s, respectively, which manifest as 0.5 th and 1.5 th harmonic disturbances in the speed [39]. The experimental results are shown in Fig. 19, where $\Delta\psi_{dh}$ and $\Delta\psi_{qh}$ are the injected flux harmonic signals, respectively. For clearer comparison, Fig. 20 presents a comparative FFT analysis of the speed under three different control methods. It can be observed that the proposed method achieves suppression performance comparable to, or even better than, the VRC in the presence of known-frequency periodic disturbances. However, when harmonic disturbances of other orders occur, the VRC, which provides suppression only at the 1st and 2nd harmonic frequencies, becomes nearly ineffective. In contrast, due to its independence from prior knowledge of harmonic orders, the ET-RBFNN enables the system to achieve excellent suppression performance even under sudden injection of uncertain periodic harmonic disturbances.

D. Experimental Results Under Variable Load Torque

Fig. 21 shows the comparative results when EC-CESO is combined with VRC and ET-ARBFNN, respectively, under a speed of 100 r/min. At 3 s, the load torque steps from 0 to

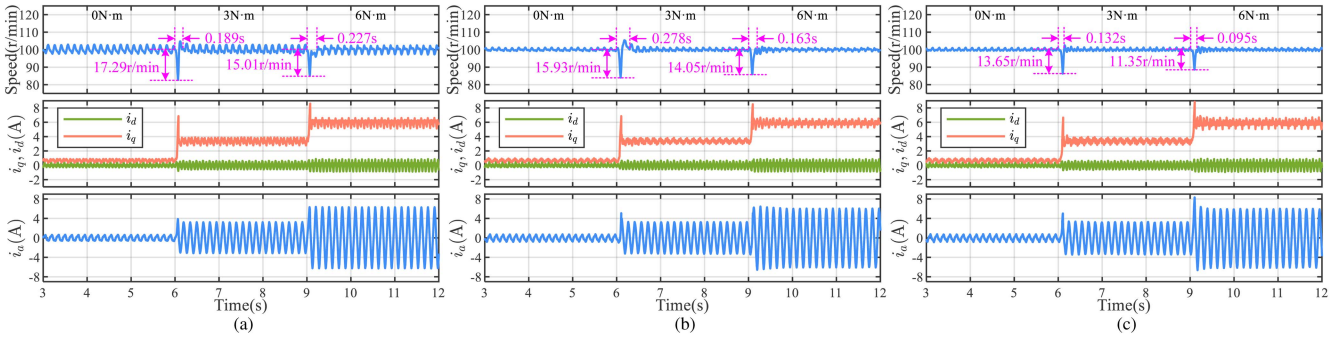

Fig. 21. Experimental results of speed, dq-axis currents, and phase-a current at 100 r/min speed under variable load torque. (a) EC-CESO. (b) EC-CESO & VRC. (c) EC-CESO & ET-ARBFNN.

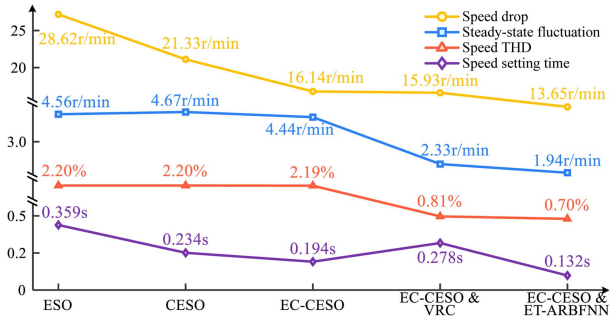

Fig. 22. Performance comparison of ESO, CESO, EC-CESO, EC-CESO & VRC, EC-CESO & ET-ARBFNN at 100 r/min under 3 N · m loads.

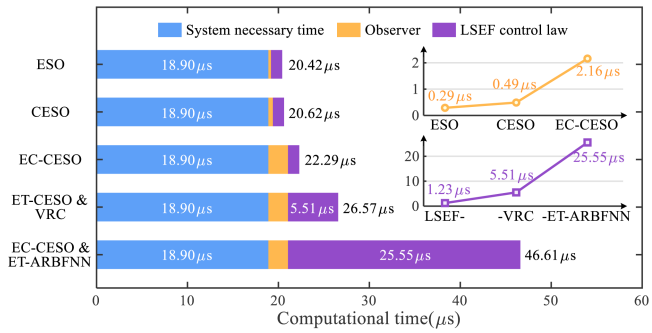

Fig. 23. Comparison of the computational burden of different methods.

3 N · m, and further increases to 6 N · m at 6 s. We can see that the introduction of ET-ARBFNN reduces the speed drop from 17.29 r/min and 15.01 r/min to 13.65 r/min and 11.35 r/min, respectively. In addition, the setting time is shortened from 0.189 s and 0.227 s to 0.132 s and 0.095 s, respectively, which indicates a significant improvement in the disturbance rejection performance of the system. In contrast, although VRC provides slight improvement in speed drop, it does not significantly reduce the setting time. In some cases, the setting time may even increase. This is due to the shift in resonant peaks caused by abrupt changes in speed during the dynamic process, which weakens the suppression capability of the VRC and, to some extent, deteriorates the dynamic performance of the system.

Based on the above experimental results, Fig. 22 compares the performance of the proposed EC-CESO & ET-ARBFNN method with other control methods at a speed of 100 r/min under a sudden load of 3 N · m. It can be found that the proposed method achieves better performance than conventional CESO and VRC in terms of speed drop, setting time, and steady-state fluctuation. In addition, it effectively suppresses noninteger harmonics with unknown frequencies, which demonstrates its superior capabilities in both aperiodic and periodic disturbance rejection.

E. Computational Burden Analysis

To evaluate the computational feasibility of the proposed methods, Fig. 23 compares the computational burden of different control methods. The computation times for ESO, CESO, and the proposed EC-CESO, mainly used for aperiodic disturbance rejection, are 0.29 μs, 0.49 μs, and 2.13 μs, respectively; while the computation times for VRC and the proposed ET-ARBFNN, used for periodic disturbance rejection, are 5.51 μs and 25.56 μs, respectively. The results show that the computation times of the proposed EC-CESO and ET-ARBFNN are significantly higher than existing methods, but their total computation time is still below the sampling period of 100 μs. Therefore, the increase in computation time can be regarded as a necessary tradeoff for achieving higher control performance through reasonable utilization of computational resources.

VII. Conclusion

In this article, a PMSM speed control method based on EC-CESO and ET-ARBFNN is proposed to suppress both aperiodic and periodic disturbances in the speed. By introducing an error correction term, the proposed method breaks the coupling relationship between zeros and poles in CESO, thereby enhancing the suppression capability against low-frequency aperiodic disturbances and reducing sensitivity to high-frequency noise in steady state. In addition, by introducing an error transformation function, the ET-ARBFNN enables the RBFNN to effectively compensate for the shortcomings of the EC-CESO in suppressing periodic harmonic disturbances using only a small number of hidden layer nodes. Experimental results demonstrate that the proposed composite control method not only suppresses both

aperiodic and periodic disturbances simultaneously, including periodic harmonics with unknown frequencies, but also exhibits less speed drop, shorter setting time, and improved dynamic response compared to conventional methods.

REFERENCES

[1] J. Yang, W.-H. Chen, S. Li, L. Guo, and Y. Yan, "Disturbance/uncertainty estimation and attenuation techniques in PMSM drives-a survey," *IEEE Trans. Ind. Electron.*, vol. 64, no. 4, pp. 3273–3285, Apr. 2017.

[2] J. Sun, S. Xu, S. Ding, Z. Pu, and J. Yi, "Adaptive conditional disturbance negation-based nonsmooth-integral control for PMSM drive system," *IEEE-ASME Trans. Mechatron.*, vol. 29, no. 5, pp. 3602–3613, Oct. 2024.

[3] Z. Sun, A. Ding, Y. Mao, C. Huang, and W. Xu, "Improved adaptive speed observer of permanent magnet linear synchronous motor with transient characteristics," *IEEE J. Emerg. Sel. Topics Power Electron.*, vol. 13, no. 2, pp. 2330–2340, Apr. 2025.

[4] W. Xu, Y. Jiang, and C. Mu, "Novel composite sliding mode control for PMSM drive system based on disturbance observer," *IEEE Trans. Appl. Supercond.*, vol. 26, no. 7, Oct. 2016, Art. no. 0612905.

[5] Y. Jiang, W. Xu, C. Mu, J. Zhu, and R. Dian, "An improved third-order generalized integral flux observer for sensorless drive of PMSMs," *IEEE Trans. Ind. Electron.*, vol. 66, no. 12, pp. 9149–9160, Dec. 2019.

[6] D.-W. Chung and S.-K. Sul, "Analysis and compensation of current measurement error in vector-controlled AC motor drives," *IEEE Trans. Ind. Appl.*, vol. 34, no. 2, pp. 340–345, Aug. 1998.

[7] D.-M. Park and K.-H. Kim, "Parameter-independent online compensation scheme for dead time and inverter nonlinearity in IPMSM drive through waveform analysis," *IEEE Trans. Ind. Electron.*, vol. 61, no. 2, pp. 701–707, Feb. 2014.

[8] J. Liu, H. Li, and Y. Deng, "Torque ripple minimization of PMSM based on robust ilc via adaptive sliding mode control," *IEEE Trans. Power Electron.*, vol. 33, no. 4, pp. 3655–3671, Jun. 2018.

[9] C. Xia, N. Liu, Z. Zhou, Y. Yan, and T. Shi, "Steady-state performance improvement for LQR-based PMSM drives," *IEEE Trans. Power Electron.*, vol. 33, no. 12, pp. 10622–10632, Dec. 2018.

[10] B. Wang, M. Tian, Y. Yu, Q. Dong, and D. Xu, "Enhanced ADRC with quasi-resonant control for PMSM speed regulation considering aperiodic and periodic disturbances," *IEEE Trans. Transp. Electr.*, vol. 8, no. 3, pp. 3568–3577, Sep. 2022.

[11] L. Li, G. Pei, J. Liu, P. Du, L. Pei, and C. Zhong, "2-DOF robust h_∞ control for permanent magnet synchronous motor with disturbance observer," *IEEE Trans. Power Electron.*, vol. 36, no. 3, pp. 3462–3472, Mar. 2021.

[12] B. Tan, Y. Cao, C. Li, C. Xia, and T. Shi, "Dual error correction extended state observer-based ADRC for PMSM speed control," *IEEE J. Emerg. Sel. Topics Power Electron.*, vol. 13, no. 5, pp. 6001–6013, Oct. 2025.

[13] H. Cao, Y. Deng, Y. Zuo, X. Liu, J. Wang, and C. H. T. Lee, "A variable structure ADRC for enhanced disturbance rejection and improved noise suppression of PMSM speed system," *IEEE Trans. Ind. Electron.*, vol. 72, no. 5, pp. 4481–4495, May. 2025.

[14] W. Xu, A. K. Junejo, Y. Liu, and M. R. Islam, "Improved continuous fast terminal sliding mode control with extended state observer for speed regulation of PMSM drive system," *IEEE Trans. Veh. Technol.*, vol. 68, no. 11, pp. 10465–10476, Nov. 2019.

[15] J. Han, "From PID to active disturbance rejection control," *IEEE Trans. Ind. Electron.*, vol. 56, no. 3, pp. 900–906, Mar. 2009.

[16] Z. Gao, "Scaling and bandwidth-parameterization based controller tuning," in *Proc. 2003 Amer. Control Conf.*, vol. 6, Jun. 2003, pp. 4989–4996.

[17] H. Cao et al., "Improved ADRC with a cascade extended state observer based on quasi-generalized integrator for PMSM current disturbances attenuation," *IEEE Trans. Transp. Electr.*, vol. 10, no. 1, pp. 2145–2157, Mar. 2024.

[18] H. Wu, C. Gan, H. Wang, S. Wang, R. Qu, and X. Liu, "Active disturbance rejection speed control with double-stage-ESO considering aperiodic and periodic disturbances for PMSM drives," *IEEE Trans. Ind. Electron.*, pp. 1–12, Jan. 2025.

[19] Y. Zuo, J. Chen, X. Zhu, and C. H. T. Lee, "Different active disturbance rejection controllers based on the same order GPI observer," *IEEE Trans. Ind. Electron.*, vol. 69, no. 11, pp. 10969–10983, Nov. 2022.

[20] S. Zhu et al., "Robust speed control of electrical drives with reduced ripple using adaptive switching high-order extended state observer," *IEEE Trans. Power Electron.*, vol. 37, no. 2, pp. 2009–2020, Nov. 2022.

[21] Y. Cui, Z. Yin, X. Cao, Y. Zhang, and Y. Liu, "Enhanced linear active disturbance rejection speed control of IPMSM based on interference differential compensation and cascaded linear extended state observer," *IEEE Trans. Power Electron.*, vol. 39, no. 10, pp. 13582–13596, Oct. 2024.

[22] Y. Cui, Z. Yin, Y. Zhang, and H. Yang, "Active disturbance rejection speed control of IPMSM drive system based on generalized multifrequency quasi-resonant filter decoupling linear extended state observer," *IEEE Trans. Power Electron.*, vol. 40, no. 8, pp. 11296–11313, Aug. 2025.

[23] J. Lang, C. Tong, Y. Zheng, J. Bai, and P. Zheng, "Decoupled dead-time compensation method using revised-resonant control-based disturbance observer in PMSM drives," *IEEE Trans. Power Electron.*, vol. 40, no. 1, pp. 340–350, Jan. 2025.

[24] S. Wen, M. Dou, and D. Zhao, "An improved dpcc based on a cascade extended state observer with notch filter for PMSM current disturbance suppression," *IEEE J. Emerg. Sel. Topics Power Electron.*, vol. 13, no. 3, pp. 3603–3617, 2025.

[25] S. Fukuda and T. Yoda, "A novel current-tracking method for active filters based on a sinusoidal internal model," *IEEE Trans. Ind. Appl.*, vol. 37, no. 3, pp. 888–895, May-Jun. 2001.

[26] M. Tian, B. Wang, Y. Yu, Q. Dong, and D. Xu, "Robust adaptive resonant controller for PMSM speed regulation considering uncertain periodic and aperiodic disturbances," *IEEE Trans. Ind. Electron.*, vol. 70, no. 4, pp. 3362–3372, Apr. 2023.

[27] L. Ding, S. Li, Y.-J. Liu, H. Gao, C. Chen, and Z. Deng, "Adaptive neural network-based tracking control for full-state constrained wheeled mobile robotic system," *IEEE Trans. Syst. Man Cybern. -Syst.*, vol. 47, no. 8, pp. 2410–2419, Aug. 2017.

[28] W. Wang, Y. Ye, X. Chen, and Y. Yuan, "Adaptive high-order sliding-mode low-speed control with RBF neural network nonlinear disturbance observer for PMSM drive system," *IEEE Trans. Power Electron.*, vol. 40, no. 8, pp. 10865–10876, Aug. 2025.

[29] C. Zhao, Y. Zuo, H. Wang, and C. H. T. Lee, "Online-trained radial basis function neural network compensator for current harmonics suppression of electric drives," *IEEE Trans. Ind. Electron.*, vol. 71, no. 12, pp. 15488–15498, Dec. 2024.

[30] C. Zhao, Y. Zuo, H. Wang, H. Cao, and C. H. T. Lee, "Smooth speed control for electric drives based on adaptive RBF neural network method," *IEEE Trans. Power Electron.*, vol. 40, no. 11, pp. 16158–16168, Nov. 2025.

[31] X. Liu, Y. Deng, H. Li, H. Cao, Z. Sun, and T. Yang, "Composite control based on FNTSMC and adaptive neural network for PMSM system," *ISA Trans.*, vol. 151, pp. 198–211, May. 2024.

[32] X. Liu, Y. Deng, J. Liu, H. Cao, C. Xu, and Y. Liu, "Fixed-time integral terminal sliding mode control with an adaptive RBF neural network for PMSM speed regulation," *Control Eng. Pract.*, vol. 156, Mar. 2025, Art. no. 106236.

[33] X. Liu, Y. Deng, J. Wang, H. Li, and H. Cao, "Fixed-time generalized active disturbance rejection with quasi-resonant control for PMSM speed disturbances suppression," *IEEE Trans. Power Electron.*, vol. 39, no. 6, pp. 6903–6918, Jun. 2024.

[34] Z. Zhou, C. Xia, Y. Yan, Z. Wang, and T. Shi, "Disturbances attenuation of permanent magnet synchronous motor drives using cascaded predictive-integral-resonant controllers," *IEEE Trans. Power Electron.*, vol. 33, no. 2, pp. 1514–1527, Feb. 2018.

[35] J. Ou, Y. Liu, R. Qu, and M. Doppelbauer, "Experimental and theoretical research on cogging torque of PM synchronous motors considering manufacturing tolerances," *IEEE Trans. Ind. Electron.*, vol. 65, no. 5, pp. 3772–3783, May. 2018.

[36] J. Sun, J. Xia, S. Ding, and X. Yu, "Exact-feedback-linearization-based adaptive second-order sliding mode control design for DC-DC boost converters," *IEEE Trans. Ind. Electron.*, vol. 72, no. 5, pp. 5397–5407, May. 2025.

[37] G. Karystinos and D. Pados, "On overfitting, generalization, and randomly expanded training sets," *IEEE Trans. Neural Netw.*, vol. 11, no. 5, pp. 1050–1057, Sep. 2000.

[38] C. Wang and D. Hill, "Learning from neural control," *IEEE Trans. Neural Netw.*, vol. 17, no. 1, pp. 130–146, Jan. 2006.

[39] C. Xia, B. Ji, and Y. Yan, "Smooth speed control for low-speed high-torque permanent-magnet synchronous motor using proportional-integral-resonant controller," *IEEE Trans. Ind. Electron.*, vol. 62, no. 4, pp. 2123–2134, Apr. 2015.

Yuxin Kang was born in Shanxi, China, in 1997. He received the B.E. degree in applied physics from Taiyuan University of Technology, Shanxi, China, in 2020. He is currently working toward the Ph.D. degree in mechatronic engineering with the University of Chinese Academy of Sciences, Beijing, China, and the Changchun Institute of Optics, Fine Mechanics and Physics, Chinese Academy of Sciences, Changchun, China.

His main research interests include advanced control strategies and applications on motor drive systems.

Yongting Deng (Senior Member, IEEE) was born in Shandong, China, in 1987. He received the B.E. degree in automation from the China University of Petroleum (East China), Qingdao, China, in 2010, and the M.S. degree in mechatronic engineering and the Ph.D. degree in mechatronic engineering from the Changchun Institute of Optics, Fine Mechanics and Physics, Chinese Academy of Sciences, Changchun, China, in 2015.

He is currently a Professor with the Changchun Institute of Optics, Fine Mechanics and Physics, Chinese Academy of Sciences. He has authored or coauthored more than 70 publications in the research interests that include controller design for ac motor drives and linear motor drives, intelligent control, and high-precision machine control techniques.

Chuanlong Zhai was born in Shandong, China, in 2001. He is currently working toward the Ph.D. degree in mechatronic engineering with the University of Chinese Academy of Sciences, Beijing, China, and Changchun Institute of Optics, Fine Mechanics and Physics, Chinese Academy of Sciences, Changchun, China.

His research interests focus on the study and application of advanced control strategies, especially in the field of permanent magnet synchronous motor (PMSM) drives.

Wenjie Li was born in Anhui, China. He received the B.E. degree in mechanical engineering from Hefei University of Technology, Anhui, China, in 2023. He is currently working toward the Ph.D. degree in mechatronic engineering with University of Chinese Academy of Sciences, Beijing, China, and Changchun Institute of Optics, Fine Mechanics and Physics, Chinese Academy of Sciences, Changchun, China.

His research interests include the development of advanced control strategies and their applications in power electronics, particularly in permanentmagnet synchronous motor drives.

Haiyang Cao (Member, IEEE) was born in Shandong, China, in 1997. He received the Ph.D. degree in mechatronic engineering from the University of Chinese Academy of Sciences, Beijing, China, and the Changchun Institute of Optics, Fine Mechanics and Physics, Chinese Academy of Sciences, Changchun, China, in 2025.

He is currently a Postdoctoral Researcher with the Ningbo Institute of Materials Technology and Engineering, Chinese Academy of Sciences, Ningbo, China. From 2023 to 2024, he was a Visiting Researcher with the School of Electrical and Electronic Engineering, Nanyang Technological University, Singapore. His research interests include electric machines and drives, and advanced control strategies.

Xiufeng Liu (Member, IEEE) was born in Changchun, China, in 1998. He received the B.E. degree in vehicle engineering from Changchun University of Technology, Changchun, China, in 2020. He received the Ph.D. degree in mechatronic engineering from the University of Chinese Academy of Sciences, Beijing, China, and the Changchun Institute of Optics, Fine Mechanics and Physics, Chinese Academy of Sciences, Changchun, China, in 2025.

His research interests include ac motor drive, sliding mode control, neural network, and digital control.

Zhimin Zhang (Student Member, IEEE) was born in Shanxi, China, in 1997. He received the B.E. degree in fluid machinery and automatic control from Jiangsu University, Zhenjiang, China, in 2020. He is currently working toward the Ph.D. degree in mechatronic engineering with the University of Chinese Academy of Sciences, Beijing, China, and the Changchun Institute of Optics, Fine Mechanics and Physics, Chinese Academy of Sciences, Changchun, China.

His main research interests include advanced control theories and applications on motor drive systems.

Wei Xu (Fellow, IEEE) received the double B.E. and M.E. degrees from Tianjin University, Tianjin, China, in 2002 and 2005, respectively, and the Ph.D. degree from the Institute of Electrical Engineering, Chinese Academy of Sciences (IEECAS), Beijing, China, in 2008, all in electrical engineering.

From 2008 to 2012, he was a Post-Doctoral Fellow with the University of Technology Sydney, Ultimo, NSW, Australia, the Vice-Chancellor Research Fellow with the Royal Melbourne Institute of Technology, Melbourne, VIC, Australia, and a Japan Science Promotion Society Invitation Fellow with Meiji University, Tokyo, Japan, respectively. From 2013 to 2023, he was a Professor with the Huazhong University of Science and Technology, Wuhan, China. Since 2024, he has been a Professor with IEECAS. His research topics mainly focus on the design and control of linear machines and drives.

Dr. Xu is a fellow of the Institute of Engineering and Technology. He was the General Chair of 2021 International Symposium on Linear Drives for Industry Applications and 2023 IEEE International Conference on Predictive Control of Electrical Drives and Power Electronics. He is an Associate Editor of over ten peer-reviewed IEEE JOURNALS, including IEEE TRANSACTIONS ON INDUSTRIAL ELEACTRONICS and IEEE TRANSACTIONS ON POWER ELECTRONICS.